




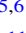
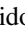








Probing the Length of the Heliospheric Tail with Energetic Neutral Atoms (ENAs) from 0.52 to 80 keV

M. Kornbleuth¹ , M. Opher¹ , K. Dialynas² , G. P. Zank^{3,4} , B. B. Wang³ , I. Baliukin^{5,6} , M. Gkioulidou⁷ , J. Giacalone⁸ , V. Izmodenov^{5,6,9} , J. M. Sokół¹⁰ , and M. A. Dayeh^{10,11} 

¹ Astronomy Department, Boston University, Boston, MA 02215, USA; kmarc@bu.edu

² Office of Space Research and Technology, Academy of Athens, 10679 Athens, Greece

³ Center for Space Plasma and Aeronomic Research (CSPAR), University of Alabama in Huntsville, Huntsville, AL 35899, USA

⁴ Department of Space Science, University of Alabama in Huntsville, Huntsville, AL 35899, USA

⁵ Space Research Institute of Russian Academy of Sciences, Profsoyuznaya Str. 84/32, Moscow, 117997, Russia

⁶ Moscow Center for Fundamental and Applied Mathematics, Lomonosov Moscow State University, GSP-1, Leninskie Gory, Moscow, 119991, Russia

⁷ Applied Physics Laboratory, Johns Hopkins University, Laurel, MD 20723, USA

⁸ Lunar & Planetary Laboratory, University of Arizona, Tucson, AZ 85721, USA

⁹ Institute for Problems in Mechanics, Vernadskogo 101-1, Moscow, 119526, Russia

¹⁰ Southwest Research Institute, P.O. Drawer 28510, San Antonio, TX 78228, USA

¹¹ University of Texas at San Antonio, San Antonio, TX 78249, USA

Received 2022 December 23; revised 2023 February 7; accepted 2023 February 14; published 2023 March 6

Abstract

The shape of the heliosphere is currently under active debate. Energetic neutral atoms (ENAs) offer the best method for investigating the global structure of the heliosphere. To date, the Interstellar Boundary Explorer (IBEX) and the Ion and Neutral Camera (INCA) that was on board Cassini provide the only global ENA observations of the heliosphere. While extensive modeling has been done at IBEX-Hi energies (0.52–6 keV), no global ENA modeling has been conducted for INCA energies (5.2–55 keV). Here, we use an ENA model of the heliosphere based on hybrid results that capture the heating and acceleration of pickup ions (PUIs) at the termination shock to compare modeled global ENA results with IBEX-Hi and INCA observations using both a long- and short-tail model of the heliosphere. We find that the modeled ENA results for the two heliotail configurations produce similar results from the IBEX-Hi through the INCA energies. We conclude from our modeled ENAs, which only include PUI acceleration at the termination shock, that ENA observations in currently available energy ranges are insufficient for probing the shape and length of the heliotail. However, as a prediction for the future IMAP-Ultra mission (3–300 keV) we present modeled ENA maps at 80 keV, where the cooling length (~ 600 au) is greater than the distance where the long- and short-heliotail models differ (~ 400 au), and find that IMAP-Ultra should be able to identify the shape of the heliotail, predicting differences in the north lobe to downwind flux ratio between the models at 48%.

Unified Astronomy Thesaurus concepts: [Heliosphere \(711\)](#); [Solar system \(1528\)](#); [Heliosheath \(710\)](#); [Heliopause \(707\)](#); [Termination shock \(1690\)](#); [Interstellar medium \(847\)](#); [The Sun \(1693\)](#); [Magnetohydrodynamics \(1964\)](#); [Magnetohydrodynamical simulations \(1966\)](#)

1. Introduction

The shape of the heliosphere is under active debate. The classic view of the heliosphere is that it has a heliotail with a long, comet-like shape (Parker 1961; Baranov & Malama 1993; Pauls et al. 1995; Zank et al. 1996). One important aspect of these models of the heliosphere was the assumption of stationarity of the solar magnetic field in the heliosheath. Opher et al. (2015) suggested that the solar magnetic field plays a critical role in organizing the solar wind plasma in the heliosheath into two jetlike structures, finding a short, croissant-like heliotail instead. Such a confinement of the solar wind in two heliospheric jets is seen in other models as well, such as in Izmodenov & Alexashov (2015) where the heliospheric jets remain within a long heliotail. Opher et al. (2021) suggested that a Rayleigh–Taylor-like instability in the heliosheath along the axis of the heliospheric jets induced by charge exchange is the probable reason for a split heliotail as

seen in Opher et al. (2015). The Rayleigh–Taylor instability leads to turbulent flows and reconnection between the heliospheric jets.

Energetic neutral atom (ENA) observations are critical for understanding the structure and shape of the heliosphere. They serve as an important tool for indirectly probing the characteristics of the global heliosphere. ENAs are created through the charge exchange of energetic ions with neutrals, and in some cases ENAs created in the heliosphere have trajectories back toward the Sun. The two primary sources for ENA observations of the heliosphere are the IBEX-Hi instrument (Funsten et al. 2009) on board the Interstellar Boundary Explorer (IBEX; McComas et al. 2009) providing data continuously from 2009 and the Ion and Neutral Camera (INCA; Krimigis et al. 2009) that was part of the Cassini mission that orbited Saturn and provided ENA data of the heliosphere from 2000 to 2017. The IBEX-Hi instrument can observe ENAs in the energy range 0.52–6 keV and INCA in the 5.2–55 keV energy range. These instruments have provided critical insights into our understanding of global heliospheric processes and primarily investigate ENAs created from pickup ions (PUIs).



Original content from this work may be used under the terms of the [Creative Commons Attribution 4.0 licence](#). Any further distribution of this work must maintain attribution to the author(s) and the title of the work, journal citation and DOI.

A number of works have discussed using ENAs from IBEX-Hi or INCA to determine the shape and extent of the heliotail. At IBEX-Hi energies, Dayeh et al. (2022) examined the evolution of the heliotail over a full solar cycle. They found that the heliotail lobes are persistent in the sky with localized variations that are directly driven by solar cycle effects. These variations result in predictable position movement for all lobes as a function of time. Furthermore, analysis revealed an asymmetry of ENA emissions in the downwind direction (see also Schwadron et al. 2014; Zirnstein et al. 2016) and the effects of multiple solar cycle phases in the tail, reflecting different ENA travel times and source histories. Reisenfeld et al. (2021) used ENA observations to map the shape of the heliosphere, and Kornbleuth et al. (2021a) used ENA modeling to compare a short- and long-tail heliosphere, and both works concluded that ENAs observed at the IBEX-Hi energies could not be used to distinguish the shape and extent of the heliotail due to the cooling length extending only about 200 au beyond the termination shock. The cooling length is defined as the distance beyond the termination shock where $1/e$ of ions of a particular energy still remain after charge exchange, which serves as a proxy for how far into the heliosphere we can probe a given line of sight (LOS) using ENAs. Dialynas et al. (2017) analyzed INCA observations that suggested that the heliosphere has a shortened tail, similar to the model of Opher et al. (2015). Comparing ENA observations from the nose and tail directions of the heliosphere, the authors found similar ENA fluxes and spectral indices for the two regions as a function of time. The authors estimated that the cooling length at energies observed by INCA (as ~ 370 au at 45 keV) suggesting that the distances out to which INCA could observe in the heliotail were sufficiently long such that the similar nose and tail fluxes indicated a short heliotail. Czechowski et al. (2020) showed that their ENA modeling, using a traditional long-tail heliosphere, could produce similar nose and tail ENA fluxes up to approximately 20 keV when only accounting for PUI acceleration at the termination shock but were unable to match the measured INCA ENA fluxes and slope of the ENA spectra. However, they did not simulate a short-tail heliosphere. Here, we aim to investigate differences in modeled ENA fluxes between a short- and long-tail heliosphere at the INCA energies.

In this work, we perform ENA modeling of long- and short-heliotail models as done in Kornbleuth et al. (2021a). The short-tail solution is based on the BU model (Opher et al. 2015; Michael et al. 2022), where the heliosphere has a croissant-like shape with two heliospheric jets bent to the tail in the north and south. The long-tail solution is based on the Moscow model (Izmodenov & Alexashov 2015, 2020), where the confinement of the solar wind in the heliosheath resembles that seen in the short-heliotail solution of Opher et al. (2015), except that the two heliospheric jets exist within a long tail. In this work, we extend the ENA model used in Kornbleuth et al. (2021a), as described in Kornbleuth et al. (2023), and use both a hybrid model of the termination shock (Giacalone et al. 2021) that captures the heating and acceleration of PUIs to infer PUI distributions from the IBEX-Hi energies to the INCA energies and a model for diffusive shock acceleration of PUIs at the termination shock (Wang et al. 2023). It is important to note that here we only calculate the acceleration of PUIs at the termination shock. There are indications (Gkioulidou et al. 2022; Kornbleuth et al. 2023) that there is an energy gap in the

energy range of ~ 4 –20 keV between modeled ENA fluxes and observations, indicating that there is likely an additional PUI acceleration mechanism in the heliosheath that is not captured by presently available models. One advantage of using the Kornbleuth et al. (2023) ENA model is the ability to compare modeled global ENA results with INCA observations, which to date has not been performed, and to investigate if heliotail differences can be discerned at these energies. In Section 2, we describe the magnetohydrodynamic (MHD) and ENA models used in this work. In Section 3, we compare the ENA results in the IBEX-Hi and INCA energy bands. In Section 4, we extend our comparison to higher energies that intersect those of IMAP-Ultra (McComas et al. 2018) to predict how the two heliotail shapes compare at energies greater than those observed to date. Finally, Section 5 is a summary of our conclusions.

2. Models

In this section we review briefly the models used in this work. For the MHD models, we use solutions from Kornbleuth et al. (2021b), which we briefly describe in Section 2.1. Additionally, we use the ENA model from Kornbleuth et al. (2023), which is based upon the model from Kornbleuth et al. (2018, 2020), and described briefly in Section 2.2.

2.1. Global Models of the Heliosphere

In this work we use the BU and Moscow kinetic-MHD models of the heliosphere from Kornbleuth et al. (2021b). The BU kinetic-MHD model is based on Opher et al. (2009, 2015) and Michael et al. (2022) and derived from the Space Weather Modeling Framework (Tóth et al. 2005). The Moscow kinetic-MHD model is based on Izmodenov & Alexashov (2015, 2020). Both models are 3D kinetic-MHD models that solve for a single-ion plasma that combines the cold solar wind plasma and hot PUIs as one fluid. The neutral particles for the two models are solved kinetically using a Monte Carlo method (Malama 1991; Izmodenov et al. 2001; Tenishev et al. 2021). The Moscow model employs a 3D moving grid to fit discontinuities that allows for no direct communication between the solar wind and interstellar medium (ISM) at the heliopause. In contrast, the BU model allows for numerical reconnection at the heliopause between the solar and interstellar magnetic fields, allowing the solar wind and ISM to interact.

Both MHD models use identical inner and outer boundary conditions from Izmodenov & Alexashov (2020). The Moscow model, while normally run with He ions, neglects He ions for a direct comparison with the BU model in this study. All the neutral and ionized populations in the ISM are assumed to have the same bulk velocity $v_{\text{ISM}} = 26.4 \text{ km s}^{-1}$ (longitude = $75^\circ.4$, latitude = $-5^\circ.2$ in the ecliptic J2000 coordinate system) and temperature $T_{\text{ISM}} = 6530 \text{ K}$ at the outer boundary, where the pristine ISM is not mediated by the heliosphere. The interstellar magnetic field intensity and orientation are assumed to be $B_{\text{ISM}} = 3.75 \mu\text{G}$ and $\alpha = 60^\circ$, implying that the magnetic field is aligned with the hydrogen deflection plane (Lallement et al. 2005) and α is the angle between the interstellar velocity and magnetic field vectors. In the ISM, the proton density is assumed to be $n_{\text{p,ISM}} = 0.04 \text{ cm}^{-3}$, and the neutral H atom density is $n_{\text{H,ISM}} = 0.14 \text{ cm}^{-3}$. These density values were chosen by Izmodenov & Alexashov (2015) because they support agreement with the following observational diagnostics: (1) distances of the termination shock in the Voyager 1

and 2 directions; (2) the density of ISM H atoms between 50 and 90 au based on PUI data and the deceleration of the solar wind at large distances; (3) the difference of the ISM H flow direction compared to the direction of the chosen pristine circumsolar interstellar magnetic field.

For the inner boundary conditions, the models use 22 yr averaged solar cycle conditions (1995–2017). Heliolatitudinal variations of the solar wind density and speed (McComas et al. 2000; Sokół et al. 2013; Tokumaru et al. 2021) are taken into account, and the temperature is related to the speed via the sonic Mach number. At Earth, a Mach number of $M = 6.44$ (corresponding to a solar wind temperature of $T_{\text{SW}} = 188,500$ K) is used. In the ecliptic plane, hourly averaged solar wind data from the OMNI 2 data set (King & Papitashvili 2005) are used for the density and speed. Heliolatitudinal variations of the solar wind speed are based on analysis of interplanetary scintillation observations (Tokumaru et al. 2012) from 1990 to 2017. For heliolatitudinal variations of the solar wind mass flux, SOHO/SWAN full-sky maps of backscattered Ly α intensities are used (Quémerais et al. 2006; Lallement et al. 2010; Katushkina et al. 2013, 2019). Data from SOHO/SWAN are available from 1995 to the end of 2017, and an inversion procedure is used to obtain the solar wind mass flux as a function of time and heliollatitude. For the solar magnetic field, a Parker solution is assumed for both models, with the radial component of the magnetic field strength being $B_{\text{SW}} = 37.5 \mu\text{G}$ at 1 au.

One important distinction between the BU and Moscow models, as noted in Kornbleuth et al. (2021b), is that the heliotail shapes and lengths are notably different. The heliotail in the BU model has a short, croissant-like shape that extends for a few hundred astronomical units in the low-latitude heliotail (Opher et al. 2015). The heliotail in the Moscow model has a long, comet-like shape that extends for thousands of astronomical units (Parker 1961; Baranov & Malama 1993; Pauls et al. 1995; Zank et al. 1996; Izmodenov & Alexashov 2003). As pointed out by Kornbleuth et al. (2021b), the plasma flow within the heliotail is remarkably similar between the two models out to approximately 400 au from the Sun. Both models show confinement of the heliosheath plasma by the solar magnetic field. Beyond a distance of 400 au, the heliotail in the BU model splits into the croissant-like shape, while in the Moscow model the two heliospheric jets stay embedded within a long tail. The BU model exhibits turbulent heliospheric jets, while the flows in the Moscow model remain laminar. As discussed in Opher et al. (2021), the turbulence in the BU model appears to originate from a Rayleigh–Taylor instability along the heliospheric jets, which is absent in the Moscow model. For the BU model, beyond 400 au in the low-latitude tail direction, there is a mixing of solar wind plasma and ISM along reconnected magnetic field lines, while the flow in the Moscow model is a pure solar wind plasma.

2.2. ENA Model

To model the ion flux at the termination shock, we follow the work of Gkioulidou et al. (2022) and find the best-fit method to match the hybrid-simulation results at the termination shock obtained by Giacalone et al. (2021). Giacalone et al. (2021) use a 2D hybrid simulation, while physical quantities such as the average proton velocity, magnetic field, electric field, and others are captured in three directions and are not confined to the simulation plane. The simulation incorporates a self-

consistent, kinetic treatment of thermal solar wind protons and PUIs, with a fluid treatment of massless, charge-neutralizing solar wind electrons. Additionally, there is an average component and a turbulent component for the initial magnetic field and bulk plasma velocity. The hybrid model is limited by the simulation domain size and time, and therefore the accuracy of the accelerated PUI spectrum decreases in accuracy around energies of 50 keV and above.

We assume a Maxwellian distribution for the transmitted and reflected PUIs, which are PUI populations energized to ~ 1 –3 keV and ~ 3 –5 keV, respectively, at the termination shock (Zank et al. 2010). We also model a PUI population, accelerated at the termination shock via diffusive shock acceleration, using a power-law distribution function (Wang et al. 2023):

$$f(v) = \frac{\xi n(\delta - 3)(q - 3)}{4\pi v_l^3(q - \delta)} \times \begin{cases} (v/v_l)^{-\delta} - (v/v_l)^{-q}, & \text{if } v_l < v \leq v_m \\ [(v_m/v_l)^{q-\delta} - 1] - (v/v_l)^{-q}, & \text{if } v > v_m \end{cases}, \quad (1)$$

where n is the reflected PUI density, ξ is the fraction of reflected PUIs accelerated at the termination shock, δ is the power-law index related to ion acceleration, and q relates the PUI acceleration to the shock compression ratio (R) via $q = 3R/(R - 1)$. Additionally, v is the individual particle velocity, and v_l and v_m are the minimum and maximum velocities for particle acceleration at the termination shock. The detailed derivation and discussion of Equation (1) can be found in Wang et al. (2023).

The method for determining the parameters used for the ENA model and the parameters themselves are described in detail in Kornbleuth et al. (2023). A fitting technique is used to match the total PUI distributions from the hybrid simulation of Giacalone et al. (2021) for the Voyager 2, flank, and tail directions using the distributions described above. The best-fit parameters, such as ion density and energy ratios relative to the plasma, are then extrapolated for all directions along the termination shock as a function of termination shock distance (see Equations (5)–(13) and Table 2 in Kornbleuth et al. 2023).

The ENA model used in this work is described in detail in Kornbleuth et al. (2018, 2020). Here, we present a brief overview of the ENA model. The parameters are applied at the termination shock and propagate into the heliosheath along plasma velocity streamlines. We include the energy-dependent extinction of ions along the streamline due to charge exchange using

$$\mathcal{N}(\mathbf{r}) = \int_{r_{\text{TS}}}^r \frac{n_{\text{H}}(\mathbf{r})\sigma_{\text{ex}}(E)v_i(E)ds}{u_p(\mathbf{r})}, \quad (2)$$

where r_{TS} is the streamline distance to the TS, n_{H} is the neutral H density, σ_{ex} is the charge-exchange cross section (Lindsay & Stebbings 2005), v_i is the speed of the parent solar wind proton that yields an ENA of a particular energy, u_p is the bulk plasma speed, and ds is the path length over which we integrate the streamline. We define the energy (E) by the parent ion energy because at the energies modeled here the parent ion velocity is much larger than the velocity of an interstellar neutral ($v_i \gg v_{\text{H}}$). The newly formed heliosheath ions that replace the extinguished ions have a low characteristic energy (~ 0.1 keV),

and because we are focusing on higher-energy ENAs, these newly formed heliosheath ions will contribute little, so we do not include them in our ENA modeling. However, at sufficient distances down the tail (i.e., beyond the cooling length), these are the main population of ions in the solar wind plasma.

We calculate the ENA flux along a radial LOS using

$$J(E, \theta, \phi) = \int_{r_{\text{observer}}}^{\infty} \frac{2E}{m_p^2} f_p(n_i(\mathbf{r}'(s)), T_i(\mathbf{r}'(s)), v_{\text{plasma}}(\mathbf{r}'(s))) n_H(\mathbf{r}'(s)) \sigma_{\text{ex}}(E) S(E) d\mathbf{r}'(s), \quad (3)$$

where \mathbf{r}' is the vector along a particular LOS as a function of θ and ϕ , s is the distance along the vector, m_p is the mass of a proton, and f_p is the phase-space velocity distribution. The velocity of the parent ion in the frame of the plasma is given by $v_{\text{plasma}} = |\mathbf{v}_p - \mathbf{v}_i|$, with \mathbf{v}_p and \mathbf{v}_i being the velocities of the bulk plasma and the parent proton, respectively. The ion density, n_i , is derived from the ion density fraction for a given population, while the ion temperature, T_i , is derived from the ion density and energy fraction as $T_i = E_i/n_i$. T_i is a fraction of the local MHD temperature based on the thermal pressure fraction of the ion species. We assume quasineutrality and use the approximation that the electrons have the same temperature as the thermal solar wind ions such that the proton temperature is given by (Zirnstein et al. 2017)

$$T_p = \frac{2T_{\text{MHD}}}{1 + \Gamma_{\text{SW}}}, \quad (4)$$

where T_{MHD} is the temperature given from the MHD solution and Γ_{SW} is the assumed thermal solar wind temperature fraction of the plasma (0.04 in the Voyager 2 direction).

The survival probability $S(E)$ of ENAs in our model represents the likelihood that an ENA created in the heliosheath will charge exchange prior to being observed by IBEX. We calculate the survival probability of an ENA along a radial LOS since the trajectories of H atoms with the energies modeled here are almost straight. The survival probability is given by (Bzowski 2008)

$$S(E) = \exp\left(-\int_{r_{\text{source}}}^{r_{\text{observer}}} \frac{\sigma(v_{\text{rel}})v_{\text{rel}}n_p}{v_{\text{ENA}}} dr\right), \quad (5)$$

where dr is the radial element over which we are integrating, v_{ENA} is the speed of the ENA, and v_{rel} is the relative velocity between the ENA and the bulk solar wind plasma given by (Pauls et al. 1995; Zank 1999)

$$v_{\text{rel}} = v_{\text{th},p} \left[\frac{e^{-\omega^2}}{\sqrt{\pi}} + \left(\omega + \frac{1}{2\omega} \right) \text{erf}(\omega) \right], \quad (6)$$

$$\omega = \frac{1}{v_{\text{th},p}} |\mathbf{v}_{\text{ENA}} - \mathbf{u}_p|.$$

Here, \mathbf{v}_{ENA} is the velocity of the ENA, \mathbf{u}_p is the solar wind bulk plasma velocity, and $v_{\text{th},p}$ is the thermal speed of the plasma. Unlike in Equations (2) and (3), we need to use v_{rel} since the velocities of the ENA and bulk plasma are within 1 order of magnitude for the energies modeled here. The background solar wind plasma distribution is assumed to have a Maxwellian distribution for the transit of ENAs back to the observer, a simplified assumption for the multispecies proton

distribution in the heliosheath that we use in calculating the ENA flux. We place the observer at the termination shock such that the survival-probability correction is out to 100 au. Considering the distance from the Sun, we only calculate the survival probability due to charge exchange.

To compare with IBEX-Hi energies, we use the IBEX-Hi energy transmission functions for each IBEX-Hi energy step in our modeling. For the INCA energies, we only simulate at the central energy band for each energy band (8.38, 18.00, 28.98, and 43.87 keV). This is because, unlike at the lower energies of IBEX-Hi where one needs to integrate over the detector response function, which may result in different fluxes depending on the incident spectrum, for the higher energies of INCA the central energy at the logarithmic mean is independent of the incident spectrum to a very good approximation (Westlake et al. 2020). For INCA, this was intercalibrated with the Magnetosphere Imaging Instrument, which was also on board Cassini. Therefore, for both INCA energies and at 80 keV, which we consider in Section 4, we only integrate our ENA fluxes for the central energy of each energy band.

3. ENA Model Comparisons with Observations

In Figure 1, we present an ENA comparison of the BU and Moscow models with respect to the 5 yr averaged (2009–2013) IBEX-Hi globally distributed flux (GDF) from Schwadron et al. (2014). The advantage of comparing with the GDF, which has the ENA contribution from the IBEX ribbon removed, is that it allows for the heliosheath contribution in the heliotail to be isolated (Schwadron et al. 2011; McComas et al. 2017).

One important point to emphasize is that the modeled maps in this comparison are not scaled. Previous works, such as Zirnstein et al. (2017), Kornbleuth et al. (2020), and Baliukin et al. (2020) required a scaling factor to quantitatively compare with IBEX-Hi ENA maps. As shown in Kornbleuth et al. (2023), with the addition of an accelerated PUI population at the termination shock, a scaling factor is no longer required for a direct comparison between modeled and observed maps.

For the IBEX-Hi comparison of the modeled maps, while a scaling factor is no longer being used, we note similar conclusions to Kornbleuth et al. (2021a). The BU and Moscow models produce maps that are quantitatively similar to each other and produce good agreement despite having two different heliotail configurations. The physical mechanism that limits differences between the two models at these energies is extinction of ions through charge exchange, which yields a cooling length for both models at distances down the heliotail where the plasma flows are similar. The differences in the plasma solutions between the two models largely manifest around 400 au down the tail. As can be seen in Figure 2, the viewing distances down the heliotail are around 200 au from the Sun in the IBEX-Hi range, and therefore differences cannot be distinguished.

In comparing the modeled maps to the IBEX-Hi GDF, we note similarities at the highest energies (2.73 and 4.29 keV), where there is a distinct pattern of high-latitude lobes with an enhanced ENA flux and two low-latitude lobes with a deficit of flux in the tail. For the 1.74 keV energy band, the modeled maps both present a similar profile to the higher-energy maps, whereas the observations have a centralized enhancement of ENA flux in the low-latitude tail. The reason for this discrepancy is likely the lack of solar cycle effects present in

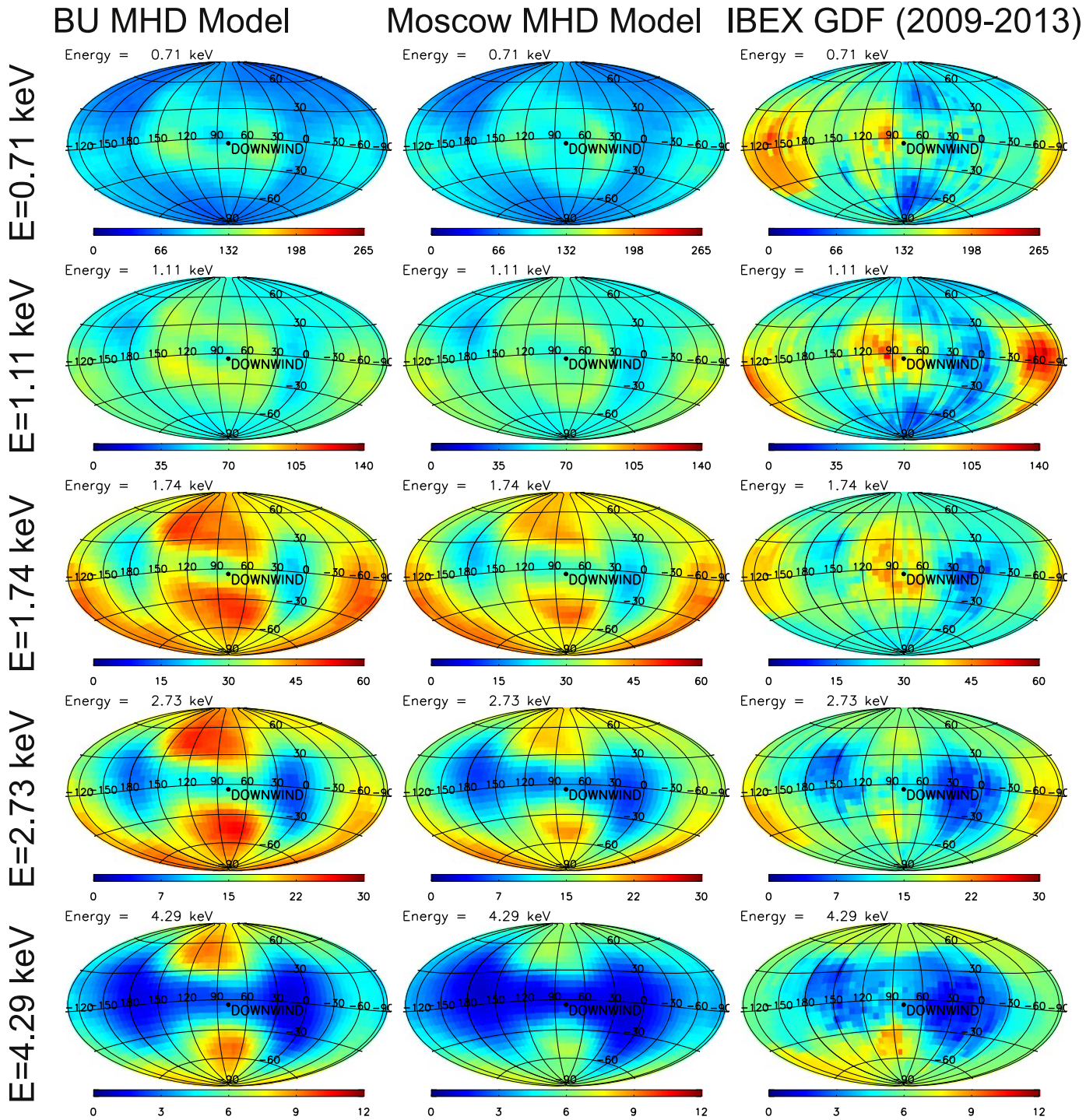


Figure 1. ENA sky maps of flux centered on the downwind (tail) direction in units of $(\text{cm}^2 \text{sr keV})^{-1}$ for the BU model (left), Moscow model (middle), and IBEX-Hi GDF from the first five years (2009–2013) of observations (right). The ENA energy band is increasing from top to bottom in all three cases. The ENA maps have a resolution of $6^\circ \times 6^\circ$ in latitude and longitude. Simulated sky maps do not use any scaling factor.

the MHD models. Since both models use steady-state solutions, the high latitudes are flooded with a higher-energy wind than should be present in reality, and therefore there is a bias of ENA flux to high latitudes at energies around 1.74 keV and above. At 0.71 and 1.11 keV, the models tend to underpredict the IBEX GDF on a global scale, which is likely also related to averaging over the solar cycle effects applied in this study and the mixing of slow and fast winds in the heliosphere. Considering we are using 22 yr average solar cycle conditions,

we are not matching with the solar wind conditions that are reflected in either the IBEX-Hi or INCA ENA observations. This can affect our comparison solely based on the solar wind conditions in the heliosheath that have been shown to affect ENA observations by IBEX-Hi (McComas et al. 2020; Galli et al. 2022) and INCA (Dialynas et al. 2017). Additionally, by using such a large solar wind averaging we remove any time-dependent phenomenon such as corotating interaction regions that would affect our comparison during solar minimum, which

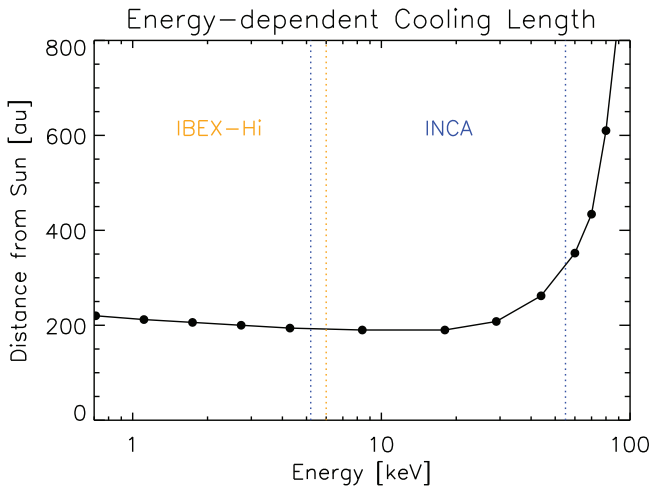


Figure 2. The distance from the Sun out to which $1/e$ ions of a particular energy remain following charge exchange with neutrals (i.e., cooling length) for the Moscow model. Included is the cooling length for the IBEX-Hi energy bands (0.5–6 keV) and the INCA energy bands (5.2–55 keV). Additionally, the cooling length at 60, 70, and 80 keV are also included. The cooling length limit in this figure is limited by the simulation box size.

is the time period reflected in our data. In a future work, we will update our model to use time-varying solar cycle conditions.

In Figure 3, we present an ENA comparison of the BU and Moscow models with respect to the 2009–2012 averaged INCA ENA maps. It should be noted that the INCA observations are not survival-probability corrected or Compton–Getting corrected because ENA emission at energies >5.2 keV becomes essentially optically thin (Dialynas et al. 2017) and the Compton–Getting factor is negligible for ENA intensities at energies >5.2 keV (Roelof et al. 2012; Dialynas et al. 2019). This paper presents the first such global ENA modeling comparison with INCA observations. The dark blue region in the INCA observations correlates with data gaps related to principal corrections to the images either due to potential contamination from Saturn’s magnetosphere or from the general direction of the Sun. The shaded regions indicate regions with low statistics due to limited viewing time.

In first comparing the BU and Moscow models at the INCA central energies of 8.38, 18.00, 28.98, and 43.87 keV, we note the similarities in the two models despite probing at higher energies. As in the higher IBEX energies, we do note some small differences in the flux levels for the different models, as described in Kornbleuth et al. (2021a, 2021b), and these can be ascribed to differences in the heliosheath plasma flows caused by different termination shock distances resulting from magnetic field draping at the heliopause of each model. As a global profile, we see similar results both quantitatively and qualitatively for both models.

In comparing the model maps to INCA observations for energies above 8.38 keV, we note the presence of two high-latitude lobes in the INCA observations similar to the model maps. Additionally, we note a deficit of ENA flux in the flanks for the model maps, correlating with the INCA basins (Dialynas et al. 2013), which appear to reflect the port and starboard lobes (McComas et al. 2013) seen in the IBEX-Hi maps. As also noted by Dialynas et al. (2013), the port lobe seen in the IBEX-Hi observations is smaller than the corresponding INCA basin, while the starboard lobe from IBEX-Hi observations is notably smaller than its corresponding

INCA basin as well. We also obtain a similar nose flux profile for the model maps and the observations.

We do observe a notable difference between the model maps and the observations in the low-latitude heliotail at the 8.38 keV energy band. This region of the heliotail is intersected by the INCA belt, which has been suggested by Dialynas et al. (2013, 2017) to originate in the heliosheath due to changes in the belt correlating with changes in the solar wind. Therefore, as in the case of the IBEX-Hi GDF, some of the model discrepancy with observations may be related to the lack of inclusion of solar cycle effects in the MHD models, where the solar wind conditions in the heliosheath likely differ from those included in our model using 22 yr averaged conditions. Considering the differences between the models and observations, and the heliosheath origin of the INCA belt, we conclude that the INCA belt is likely to be related to the further acceleration of PUIs in the heliosheath based on the comparisons noted in Gkioulidou et al. (2022) and Kornbleuth et al. (2023). This is because we utilize a hybrid model that captures PUI acceleration at the termination shock as the basis for our ENA recipe, which alone is insufficient for replicating the lower-energy channel INCA observations, and therefore further PUI acceleration beyond the termination shock (i.e., in the heliosheath) is required to match observations. Some potential sources of PUI acceleration may be adiabatic heating/cooling, acceleration due to magnetic reconnection in the heliospheric current sheet, acceleration due to turbulence in the heliosheath, or in the case of the BU model, acceleration of PUIs along field lines reconnected between the interstellar and solar magnetic fields that propagate in the region of mixed ISM and solar wind referred to as “open heliosheath” (Kornbleuth et al. 2018; Michael et al. 2018). We will explore the possible sources of acceleration leading to the INCA belt in a future study.

Another difference between the modeled and observed maps is the scaling factor required to match the INCA observations. While the use of the ENA model from Kornbleuth et al. (2023) led to the removal of the scaling factor for model maps with respect to IBEX-Hi observations, as noted in Figure 1, here a scaling factor is required especially for the 8.38 and 18.00 keV energy bands. This may well support the possibility of an as-yet-unidentified, energy-dependent acceleration mechanism for PUIs at the energy range of 4–20 keV in the heliosheath as noted by Kornbleuth et al. (2023).

Kornbleuth et al. (2023) pointed out that there is a general underprediction of the ENA flux in the modeled maps from ~ 4 to 20 keV. As described in Gkioulidou et al. (2022), an additional acceleration mechanism for PUIs is needed in the heliosheath to bridge the gap between modeled and observed ENA flux. The same effect is present in the modeled maps for the BU and Moscow models. A possible mechanism that can explain (at least partially) the data–model discrepancy is the adiabatic heating of PUIs due to the compression of decelerated plasma when it moved from the termination shock to the heliopause, which was neglected in the ENA modeling included in this work. We note that the value of n_H used in the ISM of 0.14 cm^{-3} leads to a value of 0.101 cm^{-3} for n_H immediately downstream of the upwind termination shock in the BU kinetic-MHD model. This is notably less than the New Horizons-derived value from Swaczyna et al. (2020), which predicts a density of $0.127 \pm 0.015 \text{ cm}^{-3}$. While this will affect the results of the comparison, Kornbleuth et al. (2023) noted

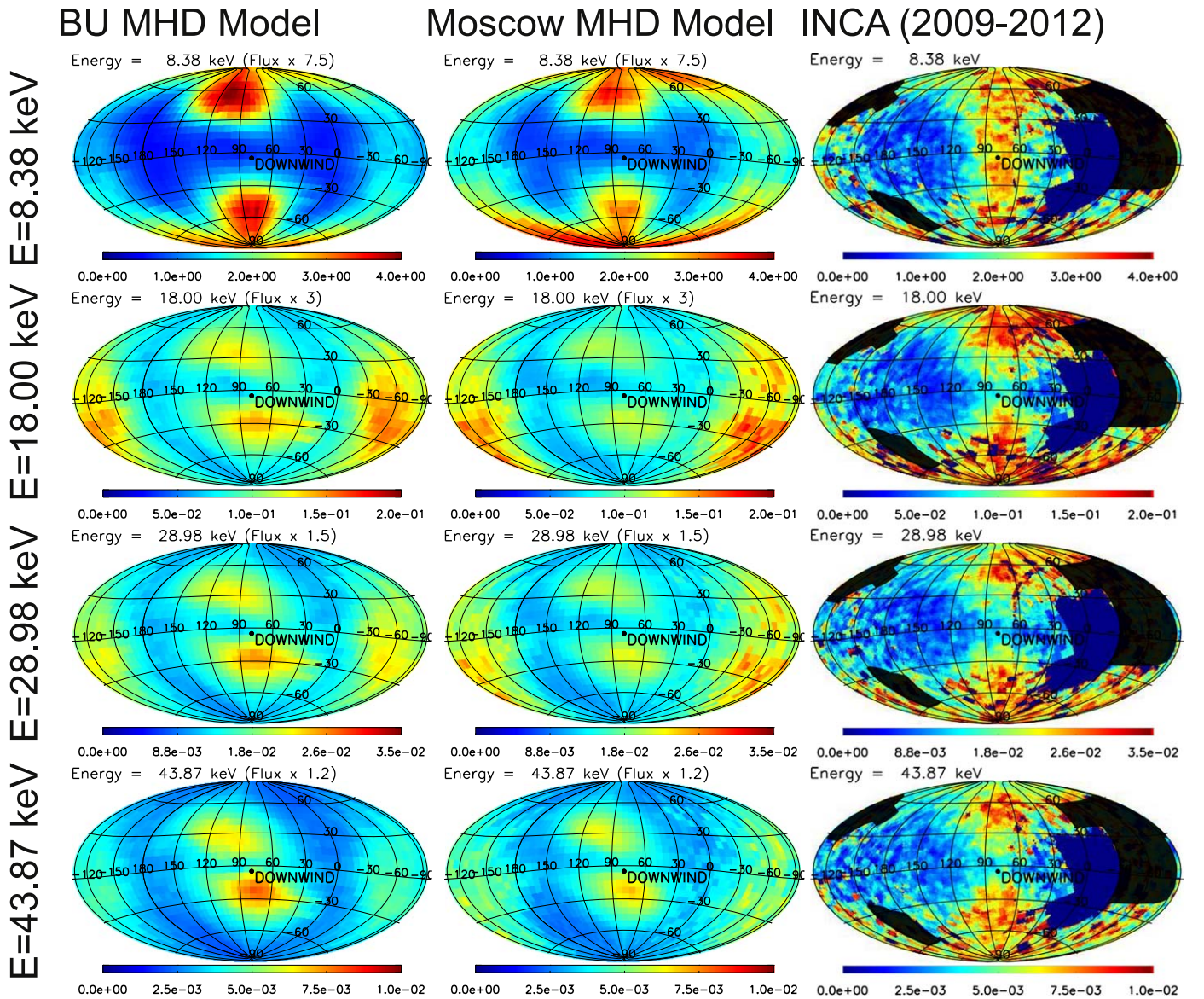


Figure 3. ENA sky maps of flux centered on the downwind (tail) direction in units of $(\text{cm}^2 \text{ sr keV})^{-1}$ for the BU model (left), Moscow model (middle), and INCA observations averaged over the years 2009–2012 (right). The ENA energy band is increasing from top to bottom in all three cases. The ENA maps have a resolution of $6^\circ \times 6^\circ$ in latitude and longitude. The dark blue region in the INCA observations correlates with data gaps related to ENA contamination from Saturn’s magnetosphere. The shaded black regions indicate regions with low statistics due to limited viewing time. From top to bottom, the simulated sky maps are scaled up using a scaling factor of 7.5, 3.0, 1.5, and 1.2, respectively.

that taking the ratio of the lower-limit and median value downstream at the upwind termination shock from Swaczyna et al. (2020) to the value from our model, the ratio ranges from 1.11 to 1.26, which is notably less than the factor of 1.8 required to quantitatively compare with observations from Kornbleuth et al. (2021b) that used the same kinetic-MHD solutions as in this work.

As described in Dialynas et al. (2017), the nose and tail ENA fluxes and the ENA spectra as a function of time is comparable at the INCA energies. This led the authors to suggest that the heliosphere could have a short tail of a few hundreds of astronomical units based on assumptions related to the cooling length (with potential uncertainty factors ranging from ~ 2 to 3 based on these assumptions). In Figure 3, we show that the nose and tail flux for both the BU and Moscow models is similar despite the Moscow model having a dramatically longer heliotail. In Table 1, we present tail-to-nose ENA flux ratios for

the BU and Moscow models. The selected regions span $84^\circ \times 84^\circ$ in the sky centered on the downwind/upwind directions (i.e., $\pm 42^\circ$ in latitude and longitude from the downwind/upwind directions). We find that the tail-to-nose ENA flux ratio for both the IBEX-Hi and the INCA energies is close to 1 for both models. The reason for these similar results is potentially the cooling length. Here we find that at the INCA energies the cooling length is still within the region where the plasma flows are similar between the short- and long-tail heliospheres modeled here (Figure 2). For Figure 2, we explicitly calculate the cooling length within our ENA model by following the streamline in the downwind direction and determining where $1/e$ of the PUIs for each energy remains following charge exchange within our model. Additionally, these results were determined using an ENA model that only included PUI heating and acceleration at the termination shock.

Table 1

Ratios of ENA Flux from the Downwind Direction to the Upwind Direction for the IBEX-Hi and INCA Energy Bands

Energy (keV)	BU MHD Model	Moscow MHD Model
0.71	1.23	1.12
1.11	1.11	1.00
1.74	1.05	0.91
2.73	1.06	0.86
4.29	1.10	0.83
8.38	1.14	0.82
18.00	0.88	0.72
28.98	0.99	0.80
43.87	1.29	1.00

Note. The selected regions span $84^\circ \times 84^\circ$ in the sky centered on the downwind/upwind directions (i.e., $\pm 42^\circ$ in latitude and longitude from the downwind/upwind directions).

PUI acceleration at distances beyond the cooling length could affect these conclusions.

4. High-energy Prediction

Due to the similarities in the modeled ENA maps for the IBEX-Hi and INCA energies, we find that these energies are insufficient for drawing conclusions on differences in the heliotail. However, this conclusion should be revisited when the acceleration of PUIs in the heliosheath is included. Therefore, we extend our ENA modeling to include an energy around 100 keV to replicate the potential for the future IMAP-Ultra instrument (McComas et al. 2018; 3–300 keV). As shown in Figure 2, for energies >60 keV there is a sufficiently long cooling length such that differences in the heliotail extent and shape should be discernible. At 70 keV, the cooling length extends as far as ~ 430 au from the Sun down the tail, which is close to where the tail splits in the BU model. By 80 keV, the cooling length is approximately 600 au from the Sun, while around 90 keV the cooling length exceeds the distance limits of our simulation. The differences in the heliotail should be discernible by IMAP from ~ 70 to 100 keV, provided that ENAs at these energies originate within the heliosheath as suggested by Dialynas et al. (2022). At these energies, the heliosheath ENA intensities should be within the dynamic range of the IMAP-Ultra instrument (Dialynas et al. 2020).

In Figure 4, we present a BU and Moscow ENA comparison at 80 keV. While the previous results used a $6^\circ \times 6^\circ$ resolution in latitude and longitude, here we use a $4^\circ \times 4^\circ$ resolution to mimic the resolution of IMAP-Ultra. We find that at this energy range, there is a noticeable difference in the two ENA profiles in the low-latitude tail. The heliotail in the BU model at low latitudes extends to approximately 400 au, after which there is a mixing of the ISM and solar wind plasmas. In the Moscow model, the heliotail extends for thousands of astronomical units and presents a laminar flow profile for the plasma without any mixing. In accordance with these different heliotail configurations, we see a distinct split in the heliotail for the BU model, whereas in the Moscow model the heliotail starts to form a more uniform profile. As such, IMAP-Ultra should be able to observe this qualitative difference to determine if the heliosphere has a short or long tail.

From the modeled maps we are able to compare the ENA flux in the high-latitude heliotail lobes relative to the region

near the downwind direction. We extract a $12^\circ \times 8^\circ$ box in longitude and latitude, respectively, over the region where the ENA flux where we discern a split in the heliotail from both the BU and Moscow results at J2000 ecliptic longitude (λ) and latitude (β) of $(\lambda, \beta) = (88^\circ \pm 6^\circ, 2^\circ \pm 4^\circ)$. Additionally, we extract the ENA flux from the area of maximum flux in the northern lobe for each model. For the BU model, this is at $(\lambda, \beta) = (108^\circ \pm 6^\circ, 10^\circ \pm 4^\circ)$, and for the Moscow model this is at $(\lambda, \beta) = (104^\circ \pm 6^\circ, 18^\circ \pm 4^\circ)$. Taking the ratio of the northern lobe flux to the low-latitude flux, we find results of 1.94 for the BU model and 1.31 for the Moscow model. Therefore, not only is a qualitative difference in the heliotail of the two models at 80 keV expected, but there is a 48% difference between the BU and Moscow models relative to the Moscow model. In contrast, performing this comparison at the highest energy band of INCA (central energy of 43.87 keV) and using the same map resolution of $4^\circ \times 4^\circ$, we find a ratio of 1.70 with the maximum flux from the northern lobe at $(\lambda, \beta) = (104^\circ \pm 6^\circ, 26^\circ \pm 4^\circ)$ for the BU model and a ratio of 1.61 with the maximum flux from the northern lobe at $(\lambda, \beta) = (100^\circ \pm 6^\circ, 30^\circ \pm 4^\circ)$ for the Moscow model. This yields a relative difference of 6% between the BU and Moscow models relative to the Moscow model, which is significantly less than the 48% difference we find at 80 keV.

5. Conclusions

In this work we perform global ENA modeling of the BU and Moscow kinetic-MHD models using the method described in Kornbleuth et al. (2023). By incorporating a PUI population accelerated at the termination shock with a power-law tail in addition to transmitted and reflected PUIs with Maxwellian distributions, we are able to bridge the quantitative gap between modeled and observed global ENA maps of the heliosphere at the IBEX-Hi energies. Unlike in Kornbleuth et al. (2021a), we no longer need a scaling factor to directly compare with IBEX-Hi ENA maps; however, the conclusion that the shape of the heliotail cannot be deduced at these energies remains unchanged.

We also present the first modeled global ENA comparison with INCA observations. While it had been suggested prior by Dialynas et al. (2017) that the similar nose and tail ENA fluxes and ENA spectral indices as a function of time observed by INCA indicated a short tail of a few hundreds of astronomical units due to a long cooling length at the INCA energies (with potential uncertainty factors ranging from ~ 2 to 3 based on these assumptions), here we find that the cooling length at the INCA energies is still within the heliotail distances out to which the BU and Moscow display differences. Therefore, given the assumptions presented in this study, our results suggest that the extent of the heliotail cannot be inferred from modeling of the INCA ENA observations using either the BU or Moscow models. However, the inclusion of a PUI acceleration mechanism in the heliosheath could affect these results. It should be noted that while Dialynas et al. (2017) found that the heliopause in the tail could extend up to ~ 200 au as an upper limit, they also noted potential uncertainties of roughly ~ 2 –3 based on their method of calculation, which could yield a heliotail extending to as much as 600 au.

With respect to INCA observations, we find general qualitative agreement with observations for the 18.00, 28.98, and 43.87 keV energy bands. For the 8.38 keV energy band, the dominating presence of the INCA belt through the low-

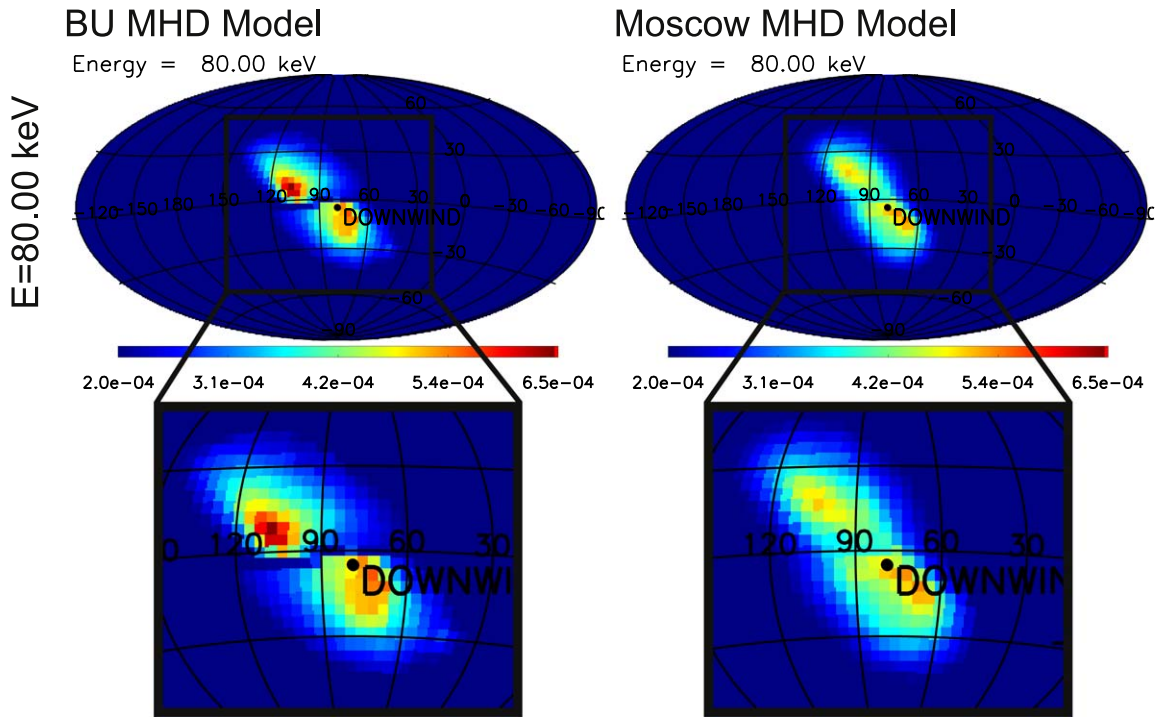


Figure 4. Simulated ENA sky maps of flux centered on the downwind (tail) direction in units of $(\text{cm}^2 \text{ s sr keV})^{-1}$ for the BU model (left) and Moscow model (right) at the 80 keV energy band. The simulated maps have a resolution of $4^\circ \times 4^\circ$ in latitude and longitude. In the bottom panels, we include a zoomed-in view of the heliotail ENAs.

latitude heliotail causes significant disagreement with model results, a profile not seen in the highest IBEX-Hi energy channel of 4.29 keV, potentially indicating the INCA belt is related to an energy-dependent PUI acceleration in the heliosheath and/or solar cycle effects that are not accounted for in the kinetic-MHD models used in this study. This need for PUI acceleration in the heliosheath also yields notable quantitative differences between modeled and observed maps, with scaling factors required to compare with INCA observations, unlike IBEX observations which no longer require a scaling factor. However, the scaling factor necessary to compare modeled ENA maps with INCA observations decreases with increasing energy.

While we are unable to differentiate between a long- and short-tail heliosphere when only PUI acceleration at the termination is considered, we expect that the inclusion of PUI acceleration in the heliosheath would enable distinction at lower energies. This is related to the fact that PUI acceleration in the heliosheath counteracts the effects of high-energy PUI depletion through charge exchange, thereby extending the depths to which we can probe the heliotail. Considering the discrepancy between our model fluxes and INCA observations, it is possible that the two models could be differentiated at INCA energies with PUI acceleration in the heliosheath included. This is a task we aim to address in a future work.

Lastly, we show a high-energy ENA map of 80 keV as a proof of concept. Since INCA energies are insufficient for distinguishing the heliotail length for the heliosheath conditions present in our steady-state kinetic-MHD models, we find that at 80 keV the cooling length is sufficiently long (>600 au) such that differences between the long- and short-tail model heliospheres can be determined. In the BU model, which exhibits a short heliotail, there is a clear split of the heliotail seen in ENA maps, while in the Moscow model, which has a

long heliotail, there is a more uniformly distributed ENA map, though high-latitude lobes of enhanced ENA flux are seen in both models.

The authors were supported by NASA grant 18-DRIVE18_2-0029, Our Heliospheric Shield, 80NSSC22M0164. M.K., M.O., and M.A.D. also acknowledge the support by NASA HGI grant 80NSSC22K0525. G.P.Z., B. W., J.G., and M.G. also acknowledge support from the NASA's Interstellar Mapping and Acceleration Probe (IMAP) under NASA contract 80GSFC19C0027. J.M.S. and M.A.D. acknowledge the partial support of a NASA IBEX grant 80NSSC20K0719. G.P.Z. and B.W. acknowledge the partial support of a NASA IBEX grant 80NSSC20K0719 subaward SUB 0000395 and from an NSF EPSCoR RII-Track-1 Cooperative Agreement OIA—2148653. K.D. also acknowledges support at JHU/APL by NASA under contracts NAS597271, NNX07AAJ69G, and NNN06AA01C and by subcontract at the Office for Space Research and Technology. I.B. and V.I. acknowledge support from the Russian Science Foundation grant 19-12-00383.

ORCID iDs

M. Kornbleuth <https://orcid.org/0000-0002-3479-1766>
M. Opher <https://orcid.org/0000-0002-8767-8273>
K. Dialynas <https://orcid.org/0000-0002-5231-7929>
G. P. Zank <https://orcid.org/0000-0002-4642-6192>
B. B. Wang <https://orcid.org/0000-0002-6000-1262>
I. Baliukin <https://orcid.org/0000-0002-8004-0904>
M. Gkioulidou <https://orcid.org/0000-0001-9979-2164>
J. Giacalone <https://orcid.org/0000-0002-0850-4233>
V. Izmodenov <https://orcid.org/0000-0002-1748-0982>
J. M. Sokół <https://orcid.org/0000-0002-4173-3601>
M. A. Dayeh <https://orcid.org/0000-0001-9323-1200>

References

- Baliukin, I. I., Izmodenov, V. V., & Alexashov, D. B. 2020, *MNRAS*, **499**, 441
- Baranov, V. B., & Malama, Y. G. 1993, *JGR*, **98**, 15
- Bzowski, M. 2008, *A&A*, **488**, 1057
- Czechowski, A., Bzowski, M., Sokół, J. M., et al. 2020, *ApJ*, **888**, 1
- Dayeh, M. A., Zirnstein, E. J., Fuselier, S. A., et al. 2022, *ApJS*, **261**, 27
- Dialynas, K., Galli, A., Dayeh, M. A., et al. 2020, *ApJL*, **905**, L24
- Dialynas, K., Krimigis, S. M., Decker, R. B., et al. 2019, *GeoRL*, **46**, 7911
- Dialynas, K., Krimigis, S. M., Decker, R. B., et al. 2022, *SSRv*, **218**, 21
- Dialynas, K., Krimigis, S. M., Mitchell, D. G., et al. 2013, *ApJ*, **778**, 40
- Dialynas, K., Krimigis, S. M., Mitchell, D. G., et al. 2017, *NatAs*, **1**, 0115
- Funsten, H. O., Allegrini, F., Bochsler, P., et al. 2009, *SSRv*, **146**, 75
- Galli, A., Baliukin, I., Bzowski, M., et al. 2022, *SSRv*, **218**, 31
- Giacalone, J., Nakanotani, M., Zank, G. P., et al. 2021, *ApJ*, **911**, 27
- Gkioulidou, M., Opher, M., Kornbleuth, M., et al. 2022, *ApJL*, **931**, L21
- Izmodenov, V. V., & Alexashov, D. B. 2003, *AstL*, **29**, 58
- Izmodenov, V. V., & Alexashov, D. B. 2015, *ApJS*, **220**, 32
- Izmodenov, V. V., & Alexashov, D. B. 2020, *A&A*, **633**, L12
- Izmodenov, V. V., Gruntman, M., & Malama, Y. G. 2001, *JGR*, **106**, 10681
- Katshkina, O., Izmodenov, V., Koutroumpa, D., et al. 2019, *SoPh*, **294**, 17
- Katshkina, O. A., Izmodenov, V. V., Quémérais, E., et al. 2013, *JGRA*, **118**, 2800
- King, J. H., & Papatashvili, N. E. 2005, *JGR*, **110**, A02104
- Kornbleuth, M., Opher, M., Baliukin, I., et al. 2021a, *ApJ*, **921**, 164
- Kornbleuth, M., Opher, M., Baliukin, I., et al. 2021b, *ApJ*, **923**, 179
- Kornbleuth, M., Opher, M., Michael, A. T., et al. 2018, *ApJ*, **865**, 84
- Kornbleuth, M., Opher, M., Michael, A. T., et al. 2020, *ApJL*, **895**, L26
- Kornbleuth, M., Opher, M., Zank, G., et al. 2023, *ApJL*, **944**, L47
- Krimigis, S. M., Mitchell, D. G., Roelof, E. C., et al. 2009, *Sci*, **326**, 971
- Lallement, R., Quémérais, E., Bertaux, J. L., et al. 2005, *Sci*, **307**, 1447
- Lallement, R., Quémérais, E., Koutroumpa, D., et al. 2010, in AIP Conference Proceedings, Vol. 1216, The Interstellar H Flow: Updated Analysis of SOHO/SWAN Data (Melville, NY: AIP), **555**
- Lindsay, B. G., & Stebbings, R. F. 2005, *JGRA*, **110**, A12213
- Malama, Y. G. 1991, *Ap&SS*, **176**, 21
- McComas, D. J., Allegrini, F., Bochsler, P., et al. 2009, *SSRv*, **146**, 11
- McComas, D. J., Barraclough, B. L., Funsten, H. O., et al. 2000, *JGR*, **105**, 10419
- McComas, D. J., Bzowski, M., Dayeh, M. A., et al. 2020, *ApJS*, **248**, 26
- McComas, D. J., Christian, E. R., Schwadron, N. A., et al. 2018, *SSRv*, **214**, 116
- McComas, D. J., Dayeh, M. A., Funsten, H. O., et al. 2013, *ApJ*, **771**, 77
- McComas, D. J., Zirnstein, E. J., Bzowski, M., et al. 2017, *ApJS*, **229**, 41
- Michael, A. T., Opher, M., & Tóth, G. 2018, *ApJ*, **860**, 171
- Michael, A. T., Opher, M., Tóth, G., et al. 2022, *ApJ*, **924**, 105
- Opher, M., Bibi, F. A., Toth, G., et al. 2009, *Natur*, **462**, 1036
- Opher, M., Drake, J. F., Zank, G. P., et al. 2021, *ApJ*, **922**, 181
- Opher, M., Drake, J. F., Zieger, B., & Gombosi, T. I. 2015, *ApJL*, **800**, L28
- Parker, E. N. 1961, *ApJ*, **134**, 20
- Pauls, H. L., Zank, G. P., & Williams, L. L. 1995, *JGR*, **100**, 21595
- Quémérais, E., Lallement, R., Ferron, S., et al. 2006, *JGRA*, **111**, A09114
- Reisenfeld, D. B., Bzowski, M., Funsten, H. O., et al. 2021, *ApJS*, **254**, 40
- Roelof, E. C., Krimigis, S. M., Mitchell, D. G., et al. 2012, in AIP Conf. Proc. Vol. 1302, Implications of Generalized Rankine-Hugoniot Conditions for the PUI Population at the Voyager 2 Termination Shock, ed. J. Heerikhuisen et al. (Melville, NY: AIP), **133**
- Schwadron, N. A., Allegrini, F., Bzowski, M., et al. 2011, *ApJ*, **731**, 56
- Schwadron, N. A., Moebius, E., Fuselier, S. A., et al. 2014, *ApJS*, **215**, 13
- Sokół, J. M., Bzowski, M., Tokumaru, M., et al. 2013, *SoPh*, **285**, 167
- Swaczyna, P., McComas, D. J., Zirnstein, E. J., et al. 2020, *ApJ*, **903**, 48
- Tenishev, V., Shou, Y., Borovikov, D., et al. 2021, *JGRA*, **126**, e2020JA028242
- Tokumaru, M., Fujiki, K., Kojima, M., & Iwai, K. 2021, *ApJ*, **922**, 73
- Tokumaru, M., Kojima, M., & Fujiki, K. 2012, *JGR*, **117**, A06108
- Tóth, G., Sokolov, I. V., Gombosi, T. I., et al. 2005, *JGRA*, **110**, A12226
- Wang, B., Zank, G. P., Shrestha, B., et al. 2023, *ApJ*, **944**, 198
- Westlake, J. H., Mitchell, D. G., Gkioulidou, M., et al. 2020, *ApJL*, **902**, L45
- Zank, G. P. 1999, *SSRv*, **89**, 413
- Zank, G. P., Heerikhuisen, J., Pogorelov, N. V., et al. 2010, *ApJ*, **708**, 1092
- Zank, G. P., Pauls, H. L., Williams, L. L., et al. 1996, *JGR*, **101**, 21639
- Zirnstein, E. J., Funsten, H. O., Heerikhuisen, J., et al. 2016, *ApJ*, **826**, 58
- Zirnstein, E. J., Heerikhuisen, J., Zank, G. P., et al. 2017, *ApJ*, **836**, 238